Nano Research 2015, 8(5): 1522–1534
DOI 10.1007/s12274-014-0637-2
Research Article
ISSN 1998-0124
CN 11-5974/O4

Solution processed MoS_2–PVA composite for sub-bandgap mode-locking of a wideband tunable ultrafast Er:fiber laser

Meng Zhang[1], Richard C. T. Howe[2], Robert I. Woodward[1], Edmund J. R. Kelleher[1], Felice Torrisi[2], Guohua Hu[2], Sergei V. Popov[1], J. Roy Taylor[1], and Tawfique Hasan[2] (✉)

[1] *Femtosecond Optics Group, Blackett Laboratory, Prince Consort Road, Imperial College London, London SW7 2AZ, UK*
[2] *Cambridge Graphene Centre, University of Cambridge, Cambridge CB3 0FA, UK*

Received: 7 August 2014
Revised: 23 October 2014
Accepted: 12 November 2014

KEYWORDS
molybdenum disulfide,
two-dimensional materials,
liquid phase exfoliation,
polymer composites,
saturable absorbers,
ultrafast lasers

ABSTRACT

We fabricate a free-standing few-layer molybdenum disulfide (MoS_2)–polymer composite by liquid phase exfoliation of chemically pristine MoS_2 crystals and use this to demonstrate a wideband tunable, ultrafast mode-locked fiber laser. Stable, picosecond pulses, tunable from 1,535 nm to 1,565 nm, are generated, corresponding to photon energies below the MoS_2 material bandgap. These results contribute to the growing body of work studying the nonlinear optical properties of transition metal dichalcogenides that present new opportunities for ultrafast photonic applications.

1 Introduction

Low-dimensional nanomaterials hold great potential for photonic applications due to their remarkable optoelectronic properties. In recent years, carbon nanotubes (CNTs) and graphene, one-(1D) and two-dimensional (2D) materials respectively, have been shown to possess a high third-order nonlinear susceptibility [1, 2] and ultrafast carrier dynamics [3, 4]. This has led to the demonstration of numerous nonlinear optical phenomena including saturable absorption [5–9], second and third harmonic generation [10, 11], and four-wave mixing [2, 12].

While graphene has attracted much research interest for photonics and optoelectronics to date [13], it is only one member of a much wider class of 2D materials,

Address correspondence to th270@cam.ac.uk

which includes, for example, quasi-2D topological insulators [14, 15] such as Bi_2Se_3 and Bi_2Te_3, transition metal dichalcogenides (TMDs), such as Molybdenum disulfide (MoS_2) [16–19] and very recently, MXenes (early transition metal carbides and carbonitrides) such as Ti_3C_2 and Ti_3CN [20]. Although experimental research into the optoelectronic properties of the latter family of materials remains at an early stage, the other 2D materials are already known to exhibit distinct and yet complementary properties to graphene, and represent equally exciting potential for photonic and optoelectronic applications [16, 17].

TMD materials, with the general formula MX_2, where M is a transition metal and X is a group VI element such as S, Se or Te, include semiconducting materials with direct bandgaps, spanning the visible spectrum [16]. MoS_2 in bulk form is an indirect-gap semiconductor with a bandgap of ~1.29 eV (961 nm) [21]. The bandgap changes as the number of layers is decreased, ultimately shifting to a direct ~1.80 eV (689 nm) bandgap [21] in mono-layers. Mono- and few-layer (i.e. <10 layers) MoS_2 exhibits high third-order nonlinear susceptibility [22–24], with Wang et al. [24] reporting values of $\mathrm{Im}(\chi^{(3)})$ for solution processed MoS_2 exceeding that of solution processed graphene for visible wavelengths: 1.38×10^{-14} esu and 1.31×10^{-13} esu for MoS_2 compared to 8.7×10^{-15} esu and 1.75×10^{-14} esu for graphene at 800 nm and 515 nm, respectively [24]. MoS_2 also displays ultrafast carrier dynamics [23, 25, 26], with a reported intraband relaxation time of ~30 fs [23] and carrier life-time of ~100 ps [26]. This is comparable to pseudo-biexponential decays experimentally observed in chemical vapor deposited (CVD) graphene on quartz substrates, a first decay with a time constant of ~150–170 fs due to cooling of hot-electron distribution via interaction with optical phonons and a second decay with time constant >1 ps due to relaxation of thermalized electron and phonon distribution [3]. This combination of properties makes MoS_2 a suitable saturable absorber (SA) for ultrafast mode-locked pulsed lasers, with the potential for pulse generation at visible wavelengths, something that is yet to be demonstrated using graphene and its derivative materials [27]. Additionally, numerous studies have considered nonlinear optical effects such as saturable and two-photon absorption in few-layer MoS_2 at near-infrared wavelengths [24, 28]. Despite photon energies lower than the material bandgap, these studies have proposed that the near-infrared saturable absorption can arise from interband states induced by defects [24, 28] such as those observed from edges of liquid phase exfoliated chemically pristine flakes of other 2D materials like graphene [29].

Like graphene [18], MoS_2 can be exfoliated through mechanical cleavage [21], solution-based methods [30–32], or grown directly by CVD [33, 34]. Mechanical cleavage produces high quality flakes ideal for fundamental studies, but is not scalable, making it unsuitable for realistic applications [18]. CVD can be used for scalable growth of mono- or few-layer MoS_2 [33–35], but it relies on high temperatures (in excess of 650 ˚C) [34], and requires additional processing steps to transfer the as-grown material on to the desired substrate [33, 35]. In contrast, solution processing of MoS_2 can be carried out under ambient conditions, and produces dispersions of mono- and few-layer flakes [30, 36] which, like graphene, can then be filtered to form films [30, 31], blended with polymers to fabricate free-standing composites [6, 30, 36, 37], or printed or coated directly onto a range of substrates [29, 38, 39]. Indeed, owing to the ease of processing and integration as well as breadth of applicability [5, 17], solution processed CNTs, graphene and MoS_2 have been used for the fabrication of photonic devices, either by coating or transfer of films onto substrates such as quartz [40, 41], mirrors [42], and optical fibers [40], or through fabrication of polymer composites [5, 6, 37, 43, 44].

Solution processing of MoS_2 can be broadly divided into two categories—intercalation, and liquid phase exfoliation (LPE). Intercalation, typically with lithium, followed by stirring or sonication in solvents, leads to the separation of MoS_2 layers from bulk crystals to produce few- and mono-layer flakes [32, 45]. However, intercalants generally cause structural alterations in the exfoliated material [45, 46], e.g., the 1T MoS_2 phase, an unstable metallic state [45]. This must be annealed at ~300 ˚C to restore the semiconducting 2H phase of pristine MoS_2 [45]. Alternatively, LPE allows exfoliation of material in a range of solvents through the use of mild ultrasonication [30, 31] without the need for chemical pre- and post-treatment, allowing production

of chemically pristine mono- and few-layer flakes.

Within the erbium gain band, tunable mode-locked lasers have been demonstrated using polymer composite SAs based on both CNTs and graphene [43, 44]. Reference [44] reported a CNT-based mode-locked laser, producing pulses as short as 2.4 ps from 1,518 to 1,558 nm, while Ref. [43] used a graphene-based SA to produce ~1 ps pulses tunable between 1,525 and 1,559 nm. To date, few-layer MoS_2-based devices have been demonstrated to Q-switch solid-state lasers at 1.06 μm, 1.42 μm and 2.10 μm to produce pulses with hundreds of nanosecond durations [28] and additionally, to mode-lock fixed-wavelength fiber lasers at 1.06 μm [40] and 1.55 μm [47, 48]. We emphasize that to date, all reports of pulsed operation of lasers utilizing MoS_2 have been at photon energies below the fundamental material bandgap, thus indicating that sub-bandgap states are likely to contribute to the absorption mechanism. We propose that the large edge-to-surface ratio of the nanoflakes in the samples give rise to interband absorbing states [49]. Indeed, lithographically textured MoS_2 single crystals have been reported to exhibit over one order of magnitude higher sub-bandgap optical absorption than that observed in the single crystals due to energy levels arising from the edge states within the bandgap [50].

Because of this edge state absorption, compared to other nanomaterial-based SAs, few-layer MoS_2 could offer wideband absorption as has been reported for graphene [8, 51]. Both these nanomaterials have enabled sub-picosecond pulse generation [8, 51]. Few-layer MoS_2 is of particular interest as it has been suggested that the material may possess a lower saturation intensity [40] and offers further optoelectronic opportunities in the visible spectral region due to the direct material bandgap of the monolayers [21].

Recently, we reported Q-switching of a fiber laser at 1,068 nm using a MoS_2–polymer composite [36]. However, for many applications such as metrology, spectroscopy and biomedical diagnostics, ultrashort picosecond pulses are required which can be tuned in wavelength. Here, we report fabrication of a free-standing MoS_2–polymer composite through exfoliation of MoS_2 crystals. The composite promotes stable self-starting mode-locking in a compact erbium-doped fiber laser cavity, and is used to demonstrate tunability from 1,535 nm to 1,565 nm, producing pulses as short as 960 fs.

2 Device fabrication

2.1 MoS_2 exfoliation and characterization

The LPE process for MoS_2 exfoliation consists of 2 steps. First, bulk MoS_2 crystals are mixed with a solvent, often with the addition of a surfactant [30, 31]. The surface energy of 2D materials such as graphene and MoS_2 is in the range of ~70 $mJ \cdot m^{-2}$ (e.g., graphene ~70 $mJ \cdot m^{-2}$ [52], MoS_2 ~75 $mJ \cdot m^{-2}$ [53]). Suitable solvents to exfoliate and stabilize LPE flakes are those with similar solvent surface energy [30, 37, 53]. However, the best-suited solvents typically have a high boiling point, which creates difficulty in materials processing [30]. For example, *N*-methylpyrrolidone (NMP), well suited to dispersing graphene [6, 37, 54] and CNTs [5] as well as MoS_2 [30, 53], has a boiling point of 202 °C [55]. For ease of handling and processing, it is thus desirable to exfoliate MoS_2 in an aqueous solution. However, the solvent surface energy of water (~100 $mJ \cdot m^{-2}$ [56]) presents too large a mismatch to support a dispersion alone and requires the addition of a dispersant such as polymer or surfactant [37, 57, 58]. The most effective surfactants for layered materials are those with a flat molecular structure (e.g., bile salts) with a hydrophobic and a hydrophilic side [37]. In this case, the hydrophobic side of the surfactant molecule adsorbs on to the surface of the flakes while the hydrophilic side creates an effective surface charge around the flake [37, 58]. This stabilizes the dispersion by producing a Coulomb repulsion between the flakes to prevent reaggregation [31, 37, 58]. We thus use sodium deoxycholate (SDC) bile salt surfactant, which has previously been effectively used to exfoliate graphene [37]. The second step is to apply ultrasound, which exfoliates the material by creating local pressure variations sufficient to overcome the weak van der Waals forces between the atomic layers of the bulk crystal [30, 37], producing a dispersion enriched in few- and mono-layer flakes [30]. We prepare the MoS_2 dispersion by ultrasonicating 120 mg of MoS_2 crystals (Acros Organics, 6 μm) with 90 mg of SDC in 10 mL of deionized water for 2 hours

at ~5 ˚C. The resultant dispersion is centrifuged for 1 hour at ~4,200 g in a swinging bucket rotor. This acts to sediment the un-exfoliated material as larger flakes descend more rapidly through the centrifuge cell than the exfoliated few-layer flakes [59]. The upper 80% of the dispersion, which now primarily contains few- and mono-layer flakes, is decanted for analysis and composite fabrication. The inset to Fig. 1(a) shows a photograph of a cuvette containing 10 vol.% diluted MoS_2 dispersion.

The optical absorption (OA) spectra of the dispersions are measured using a UV/vis spectrometer with 1 nm steps. The OA spectrum of the MoS_2 in the dispersion, diluted to 10 vol.%, is shown in Fig. 1(a). The two absorption peaks at ~665 nm and ~605 nm result from the A and B excitonic transitions [60, 61], while those at ~440 nm and ~395 nm are due to the C and D transitions between higher density of state regions of the band structure [60, 61]. The peak assignments are according to the common nomenclature used to denote absorption peaks from higher to lower wavelengths [62]. We use OA spectroscopy to estimate the concentration of exfoliated MoS_2 flakes via the Beer–Lambert Law,

$$A_\lambda = \alpha_\lambda c l$$

where c is the concentration (g·L^{-1}), l is the absorption length (m), α_λ is the absorption coefficient (L·g^{-1}·m^{-1}) and A_λ the absorption at wavelength λ. We calculate α for wavelengths corresponding to the above-mentioned excitonic absorption peaks: 665 nm (A), 605 nm (B) and additionally for 672 nm (allowing comparison with Refs. [30, 63]) and 800 nm (a featureless region of the spectrum) from a MoS_2 dispersion of known concentration measured experimentally. We use a stable dispersion of MoS_2 prepared in cyclohexanone solvent using the LPE method described above. This allows exfoliation without the use of surfactant, reducing the error in the residual mass measurement. We first measure the residual mass of MoS_2 from a known volume of MoS_2 dispersion for 5 samples (~100 μL volume, average mass 94.29 mg, standard deviation 0.6 mg) in a TA instruments Q50 Thermogravimetric Analyzer (TGA) with 0.1 μg measurement resolution. Note that the higher standard deviation is due to quick evaporation of solvent in the TGA crucible at the start of experiment. Figure 1(b) plots the TGA data for 5 separate measurements with the associated temperature profile. The dispersions are heated at a constant rate under an N_2 enriched atmosphere. The mass of each sample decreases from ~95 mg at RT to

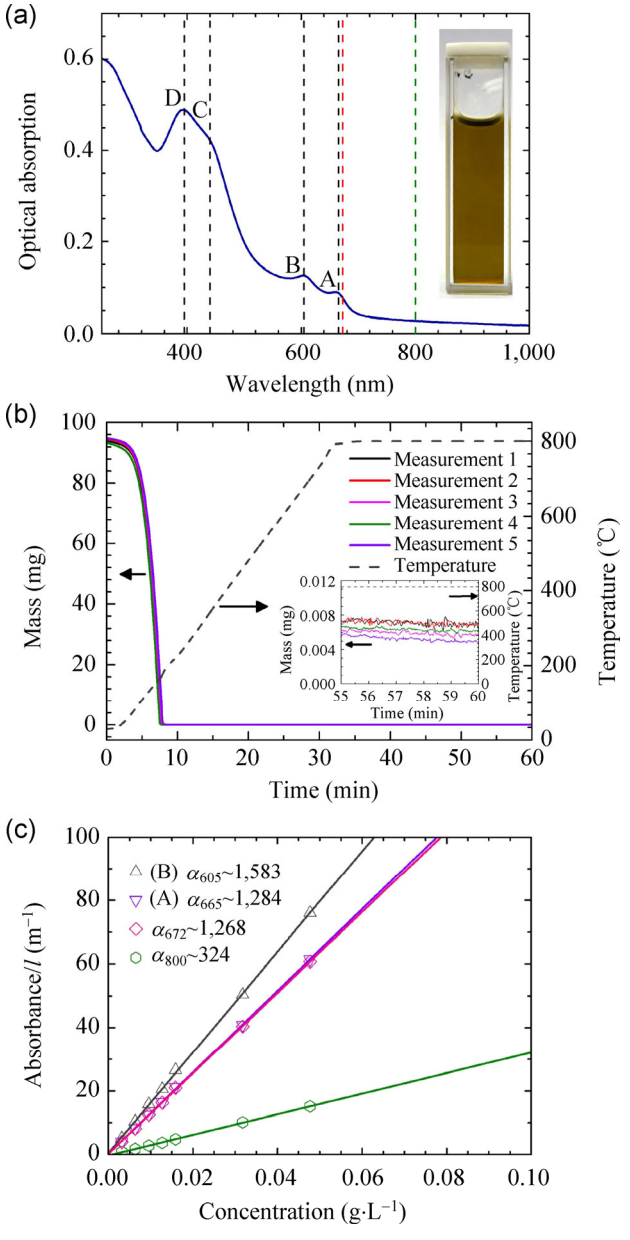

Figure 1 Optical absorption characterization of the MoS_2 dispersion used for composite fabrication. (a) Absorption spectrum of the dispersion diluted to 10 vol%. The dashed lines indicate the wavelengths used for the calculation of the absorption coefficient for MoS_2, α. Inset: photograph of a cuvette of the undiluted dispersion. (b) TGA plot of five MoS_2 dispersions in cyclohexanone with associated temperature profile. Inset: stabilized MoS_2 mass at 800 ˚C. (c) Calculation of α for 605, 665, 672 and 800 nm, given by the respective gradients.

residual MoS_2 mass at 800 ℃. The temperature is kept at 800 ℃ until the residual MoS_2 mass is stabilized; see inset. We choose 800 ℃ for two reasons. First, MoS_2 is stable at this temperature. Second, though cyclohexanone (155.6 ℃ boiling point [64]) completely evaporates at ~170 ℃, we find that 800 ℃ is required to decompose the solvent impurities. This strategy thus ensures accurate measurement of the amount of the dispersed MoS_2 flakes (average residual mass 6.36 μg for the five samples). We next measure the optical absorbance of a series of diluted MoS_2 dispersions derived from the abovementioned dispersion. Plotting A/l against c, as shown in Fig. 1(c), produces straight-line fits, with gradient (i.e. α_λ values): α_{605} = 1,583 L·g^{-1}·m^{-1}, α_{665} = 1,284 L·g^{-1}·m^{-1}, α_{672} = 1,268 L·g^{-1}·m^{-1} and α_{800} = 324 L·g^{-1}·m^{-1}. Note that our estimated α_{672} is at the lower range of previously reported values, between 1,020 L·g^{-1}·m^{-1} [63] and 3,200 L·g^{-1}·m^{-1} [30]. The residual mass reported in Refs. [30, 63] was calculated from measurement of filtered films of MoS_2 which may introduce errors in the estimation of α. Using our calculated values of α at these four wavelengths, we estimate the MoS_2 concentration in aqueous dispersion is ~0.07 g·L^{-1}.

The MoS_2 flakes are characterized by scanning transmission electron microscopy (STEM), and atomic force microscopy (AFM). For STEM imaging, the dispersion is deposited onto a holey carbon grid, and then rinsed with deionized (DI) water. This removes the excess surfactant, leaving the isolated flakes on the grid. The prepared grid is imaged with an FEI Magellan SEM at 20 kV, using an STEM detector. The distribution of flake sizes is shown in Fig. 2. The average flake dimensions (50 flakes measured) are 220 nm ± 20 nm for the long axis and 110 nm ± 10 nm for the short axis; see Figs. 2(a) and 2(b), respectively.

Samples for AFM are prepared by drop-casting diluted dispersions onto a Si/SiO_2 wafer, followed by rinsing with DI water to remove the surfactant. The sample is imaged with a Bruker Dimension Icon AFM in ScanAsyst™ mode, using a silicon cantilever with a silicon nitride tip. Figures 3(a) and 3(b) show micrographs of typical flakes, associated height variations (Fig. 3(c) and 3(d)) along the marked lines, and the distribution of flake thicknesses, shown in Fig. 3(e). We measure 58% of flake thicknesses to be in

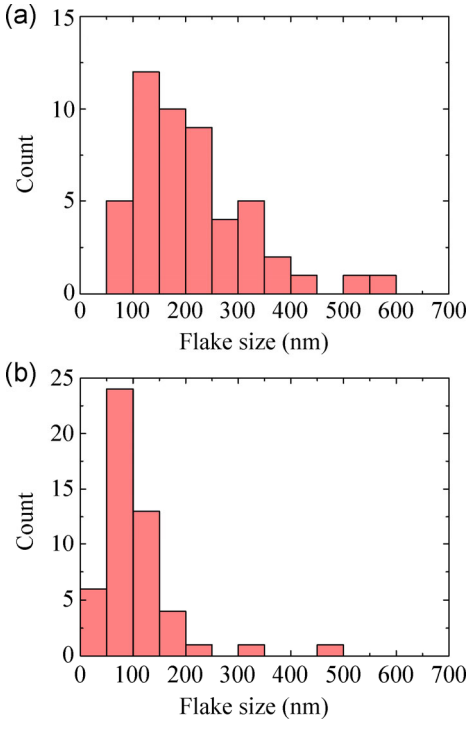

Figure 2 TEM distribution of the MoS_2 flakes deposited on a holey carbon grid along lateral dimensions for the (a) short axis and (b) long axis.

the 2–4 nm range, corresponding to ~4–6 layer thick flakes, assuming ~1 nm measured thickness for a monolayer flake and ~0.7 nm increase in thickness for each additional layer [65].

We next characterize the dispersed flakes using Raman spectroscopy. This is one of the most widely exploited non-destructive methods for characterizing the vibrational modes and hence the structure of nanomaterials. There are two main peaks located close to 400 cm^{-1} in the spectrum of both few-layer and bulk MoS_2, corresponding to the in plane (E^1_{2g}) and out of plane (A_{1g}) vibration modes [65–67]. The positions of these two peaks vary with changing number of MoS_2 layers [65, 66]. A_{1g} blue-shifts [65, 66] by ~4 cm^{-1} with increasing layer count (mono- to six-layer) as the interlayer van der Waals forces stiffen the vibration mode in thicker samples [65]. Meanwhile, E^1_{2g} red-shifts [65, 66], by ~2 cm^{-1} (mono- to six-layer), due to increased dielectric screening of the interlayer Coulomb interactions, leading to softening of the mode [68]. For mono-layer to bulk transition, this becomes ~4–5 and ~2–3 cm^{-1} [65]. The transition leads to a progressive increase in the difference between the peak positions

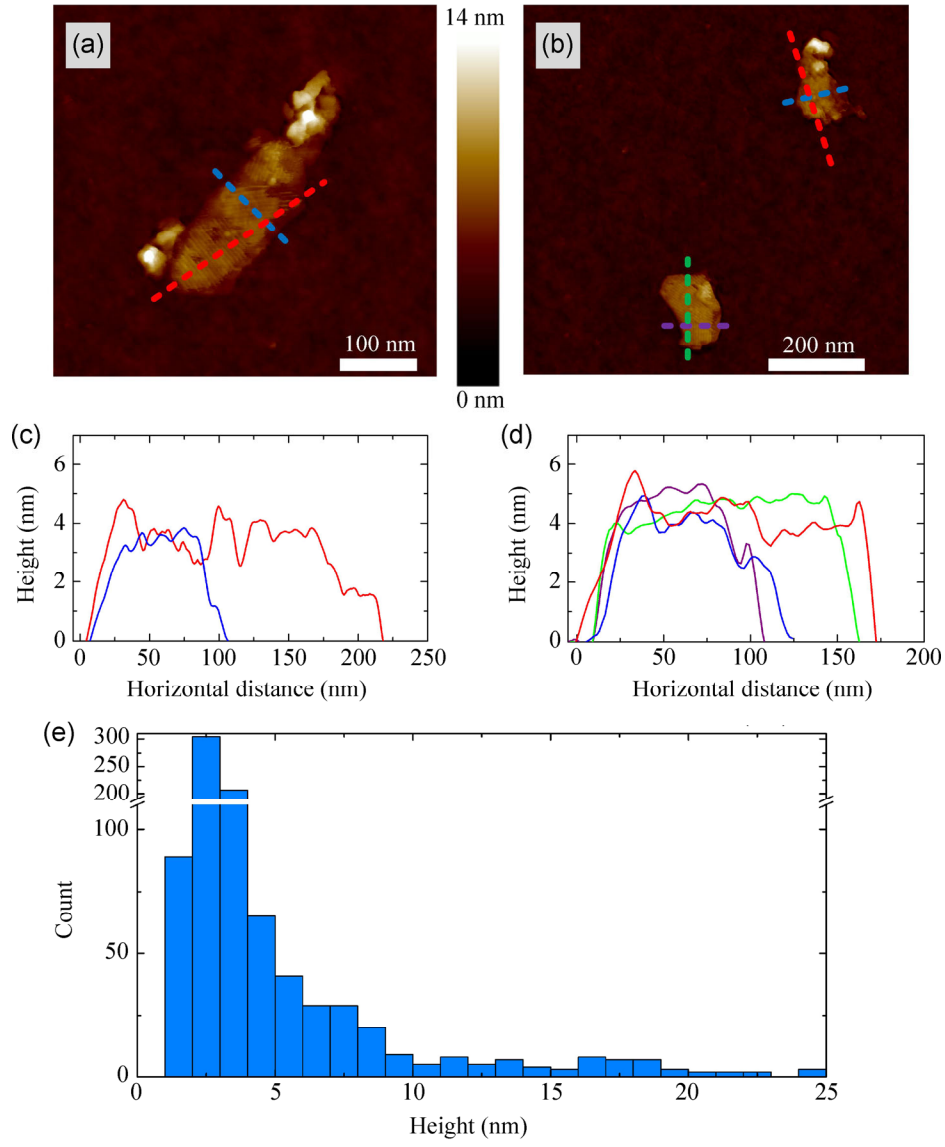

Figure 3 AFM characterization of the dispersed MoS_2 flakes. (a, b) AFM images of typical MoS_2 flakes deposited on Si/SiO_2. (c, d) Height variations of the flakes along the marked lines. (e) Statistical distribution of flake thicknesses obtained by AFM.

(Δw) from 18.7 cm^{-1} for mono-layers to 25.5 cm^{-1} for bulk MoS_2 [65, 66]. Between mono- and bi-layer flakes, Δw increases by ~3 cm^{-1} [65], with progressively smaller shifts for subsequent layer count increases, reaching ~25 cm^{-1} for six-layer flakes [65]. Therefore, Δw can be used to assess the number of layers in a MoS_2 sample [65, 66]. The dispersed MoS_2 flakes are prepared as discussed above for AFM measurements. The spectra are collected with a Renishaw 1,000 at 514.5 nm with an incident power of ~1 mW. The spectra for bulk MoS_2 and for the exfoliated flakes are shown in Fig. 4(a). The two peaks for the drop-cast sample are measured at 384.06 $cm^{-1} \pm 0.01$ cm^{-1} (E^1_{2g}) and 408.68 $cm^{-1} \pm 0.01$ cm^{-1} (A_{1g}), giving Δw = 24.62 $cm^{-1} \pm 0.02$ cm^{-1} from ~30 measurements across the sample. The bulk sample shows peaks at 383.73 $cm^{-1} \pm 0.02$ cm^{-1} (E^1_{2g}), and 409.02 $cm^{-1} \pm 0.02$ cm^{-1} (A_{1g}), resulting in Δw = 25.29 $cm^{-1} \pm 0.03$ cm^{-1}. This reduction in Δw for the exfoliated sample indicates the presence of few-layer MoS_2 flakes, estimated to be of 4–6 layers. The Raman results thus confirm our AFM measurements.

2.2 MoS_2–polymer composite fabrication

The free-standing MoS_2–polymer composite film is

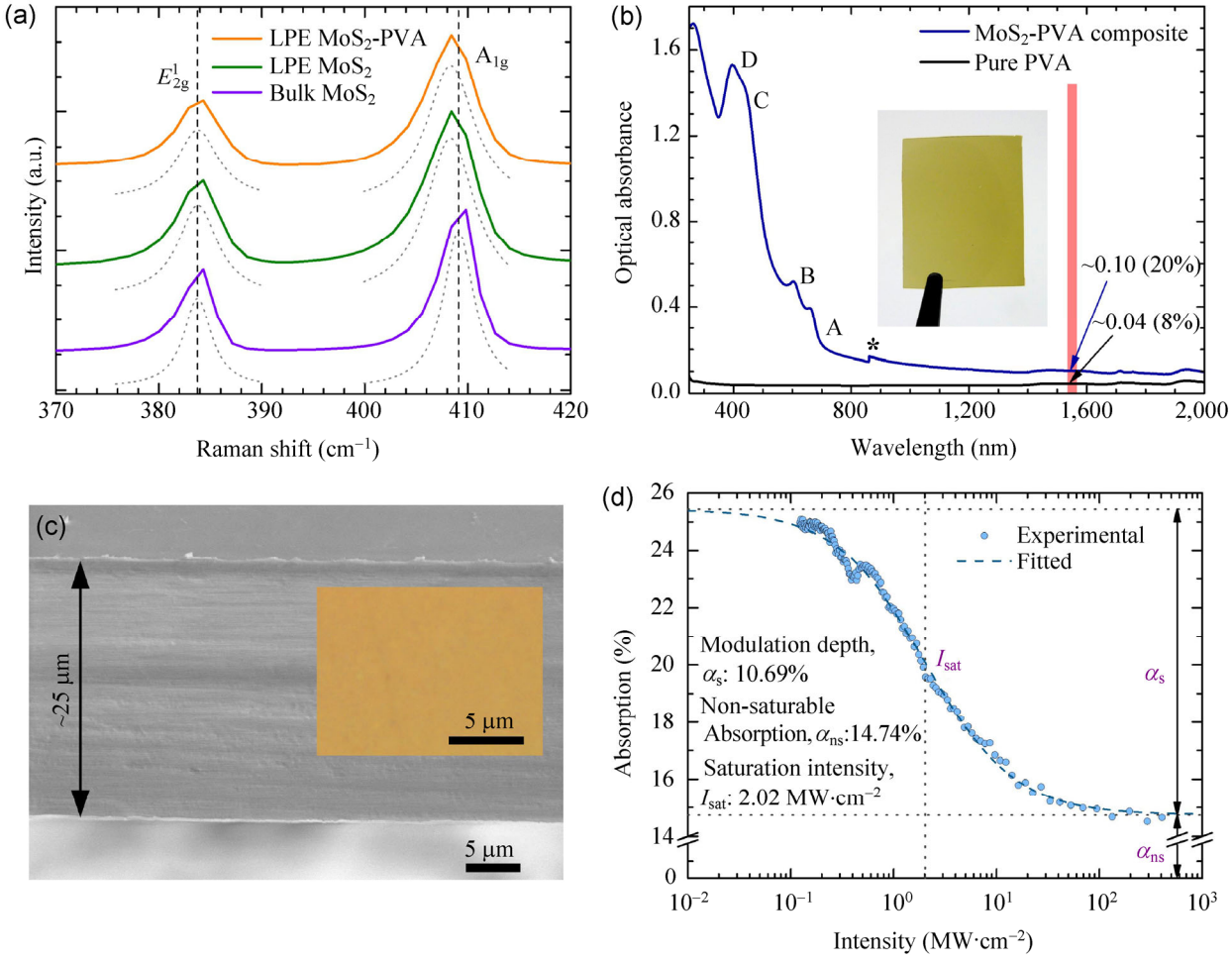

Figure 4 Characterization of the MoS_2-polymer composite film. (a) Raman spectra of the bulk MoS_2 crystal, LPE MoS_2 on Si/SiO_2 and the MoS_2-polymer composite film. The vertical dotted lines indicate the peak positions obtained from Lorentzian fitting of the bulk MoS_2 peaks (dotted grey lines, vertically shifted), showing the differences in peak positions. (b) Linear optical absorption of the MoS_2-PVA saturable absorber composite and pure PVA film of same thickness, indicating absorption from MoS_2 in the sub-bandgap region. Corresponding % transmission values are also indicated. The shaded area defines the tunable range of the laser operation. The * symbol indicates change of grating in the spectrometer. Inset: photograph of the free-standing film. (c) SEM and optical micrograph (inset) image showing no aggregation/defect in the composite. The film thickness is ~25 μm. (d) Nonlinear optical absorption of the MoS_2-PVA composite, measured via an open-aperture Z-scan at 1,565 nm (~0.8 eV).

prepared by mixing 4 mL of ~0.07 g·L^{-1} MoS_2 dispersion with 2 mL of 15 wt.% aqueous polyvinyl alcohol (PVA) solution. The MoS_2–PVA mixture is poured into a petri-dish and dried at ~20 ℃ to form a ~25 μm thick free-standing composite film. Figure 4(b) shows the linear absorption spectrum of the MoS_2 composite. For comparison, absorption spectrum from a pure PVA film of same thickness is also presented. Assuming negligible scattering contribution, the difference in absorbance (0.04 vs. 0.1) indicates sub-bandgap absorption from MoS_2 flakes in the composite. The shaded region highlights the operating region of our tunable laser, confirming that mode-locking occurs at photon energies below the bandgap. Optical microscopy is a common technique to verify nanomaterial based SA composite films [5]. The optical micrograph, shown in the inset to Fig. 4(c), confirms the lack of >1 μm aggregates, which would otherwise have resulted in large scattering losses [69].

The cross-section of the 25 μm composite film is imaged using an FEI Magellan Scanning Electron Microscope (SEM), see Fig. 4(c). The film is sliced using

a Leica Ultracut UCT. As with the optical micrograph, no aggregates are visible in the cross-section image, confirming that the flakes are uniformly distributed in the polymer composite.

The Raman spectrum of the composite film is measured as above for the dropcast material for ~30 points. The spectrum is shown in Fig. 4(a). The peaks are located at 383.79 $cm^{-1} \pm 0.02\ cm^{-1}$ (E^1_{2g}) and 408.28 $cm^{-1} \pm 0.02\ cm^{-1}$ (A_{1g}). The absence of a noticeable shift in the peak positions from those measured for the exfoliated MoS_2 indicates that the material structure is unaffected by its inclusion in the composite. Finally, the nonlinear absorption of the sample is measured using an open aperture Z-scan [70] with a 750 fs pulse source, centered at a wavelength of 1,565 nm with a repetition frequency of 17.8 MHz. The absorption as a function of intensity (Fig. 4(d)), $\alpha(I)$, is well fitted by the two-level saturable absorber model [71]:

$$\alpha(I) = \alpha_s / (1+ I/I_{sat}) + \alpha_{ns},$$

where I is intensity of the input optical pulse, $\alpha(I)$ is the intensity-dependent absorption, α_s and α_{ns} are the saturable absorption and non-saturable absorption component, respectively and I_{sat} is the saturation intensity (the intensity necessary to reduce the saturable absorption component by a half) [72]. From the fit, we extract the modulation depth (i.e., saturable loss), α_s = 10.69%, saturation intensity, I_{sat} = 2.02 $MW \cdot cm^{-2}$ and non-saturable absorption, α_{ns} = 14.74%.

3 Wideband tunable ultrafast Er:fiber laser using MoS_2–PVA composite

We use this free-standing MoS_2–polymer composite to build and test an ultrafast laser. We develop an erbium (Er)-doped fiber laser consisting of all-fiber integrated components for an alignment-free and compact system, as shown in Fig. 5. An Er-doped fiber amplifier module (IPG EFB-20-ps, with a 1 m double-clad active fiber pumped by a multimode laser diode) was used to provide amplification at ~1.55 μm, followed by an inline polarization-independent optical isolator to ensure unidirectional propagation. A wavelength-tunable filter with 12.8 nm bandwidth was used to select the lasing wavelength of the cavity. The pass-band filter angle is controlled by a micrometer screw, providing continuous tunability from 1,535 to 1,565 nm. The MoS_2 SA is integrated into the fiber laser cavity by sandwiching a ~1 mm × 1 mm piece of the composite between two fiber connectors, adhered with index matching gel. The output signal is delivered through a 15:85 fused-fiber output coupler (OC) to both spectral and temporal diagnostics. The addition of a polarization controller (PC) enables adjustment of the polarization state within the cavity, but is not fundamental to the mode-locking action. The total cavity length is 15.4 m.

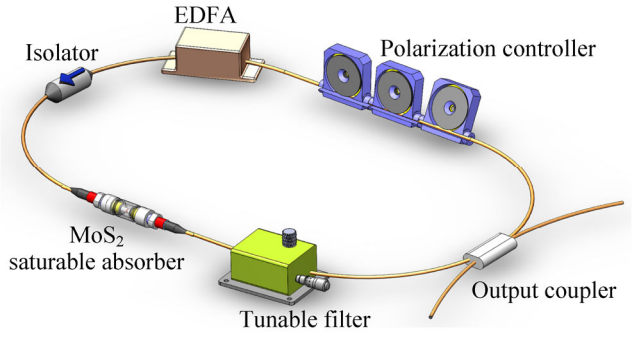

Figure 5 Schematic of the wideband tunable ultrafast Er:fiber laser. EDFA: erbium-doped fiber amplifier.

Self-starting mode-locking is observed at the fundamental repetition frequency of the cavity of 12.99 MHz, with 65 pJ pulse energy. From Fig. 2, we note that the lateral dimensions of the majority of MoS_2 flakes is ~100–200 nm, resulting in a large edge to surface area ratio. We suggest that in spite of operating at below the material bandgap, our device initiates mode-locking because of saturable absorption from the edge-related sub-bandgap states [49, 50]. The output wavelength is tunable from 1,535 to 1,565 nm (as shown in Fig. 6). This tuning range is limited by the gain bandwidth of the Er-doped fiber amplifier module and tunable filter. The full width at half maximum (FWHM) spectral bandwidth varies from ~3.0 to ~0.4 nm. The net cavity group velocity dispersion (GVD) is anomalous, facilitating soliton pulse shaping through the interplay of GVD and self-phase modulation (SPM). This is confirmed by the observation of narrow peaks superimposed on the soliton-pulse spectrum—arising from resonances between the soliton and dispersive wave components emitted after soliton perturbations—for various wavelengths within the tuning range (e.g.

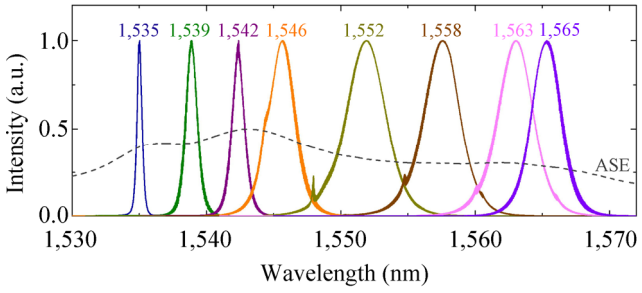

Figure 6 Output spectra at eight representative wavelengths, continuous tuning from 1,535 nm to 1,565 nm. The amplified spontaneous emission (ASE) band of the amplifier is also shown (dashed).

1,552, 1,558 and 1,563 nm in Fig. 6). However, sidebands are not observed at all lasing wavelengths when the characteristic soliton length, which scales with its characteristic duration, becomes long compared to the length of the cavity [73]. Figure 7 shows five representative autocorrelation traces, at the wavelengths of 1,535, 1,542, 1,552, 1,557, and 1,565 nm, measured using an intensity autocorrelation, and all well fitted with a sech^2 shape—the temporal pulse profile expected from the theory of optical fiber solitons [74]. At wavelengths above ~1,550 nm, the laser produces ultrashort pulses with ~1 ps duration. Pulses at shorter wavelengths of 1,535 nm and 1,542 nm, are longer with 7.1 ps and 3.9 ps duration, due to the overlap between the edge of the amplified spontaneous emission (ASE) spectrum and tunable filter pass-band, leading to a narrower pulse spectrum and consequently, a longer pulse.

Figure 8 summarizes the laser pulse characteristics within the tuning range. The shortest pulse duration (960 fs) is achieved at a wavelength of 1,552 nm (Fig. 8(a)), with a corresponding FWHM spectral bandwidth of 3.0 nm. The time–bandwidth products (TBP) at different wavelengths range from 0.37 to 0.47 as shown in Fig. 8(b). The small deviation from the transform-limited TBP for sech^2 pulses of 0.315, indicates a low chirp. This small chirp suggests that a reduction in pulse duration would be possible by managing the dispersion of the cavity. The output power could also be scaled by chirped pulse amplification, resulting in higher pulse energies, since the output of the pulsed laser is limited by a measured MoS_2 SA damage threshold of 0.1 mW/μm^2 average intensity, attributed to thermal degradation of the host polymer. Note that the damage threshold of the SA could also be improved by using printed or spray-coated, substrate-bound MoS_2 SAs without the host polymer on glass or quartz substrates. However investigation of different SA fabrication methods is beyond the scope of this manuscript.

Laser stability is inferred from the radio frequency (RF) spectra [75]. The RF spectra for our laser at 1,552 nm are shown in Fig. 9. The fundamental frequency, presented in Fig. 9(a), recorded on a span of 50 kHz, shows a high signal to background extinction ratio of ~55 dB. Figure 9(b) shows higher cavity harmonics, recorded on a span of 90 MHz, without any noticeable sign of Q-switching instabilities, indicating good mode-locking performance of the cavity [75]. Similarly stable performance is observed throughout the tuning range of the laser.

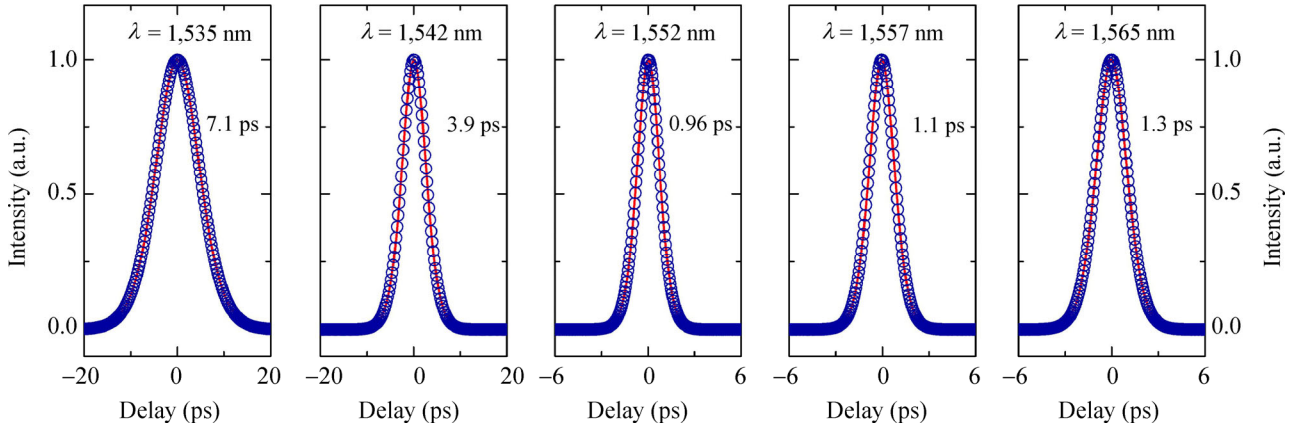

Figure 7 Autocorrelation traces of the laser output at five representative wavelengths within the tunable operating range.

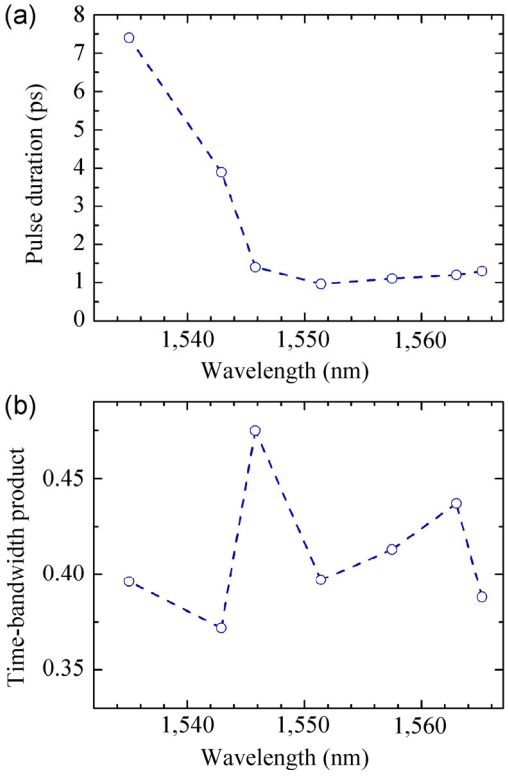

Figure 8 Output pulse duration (a) and time-bandwidth product (b) as a function of the wavelength.

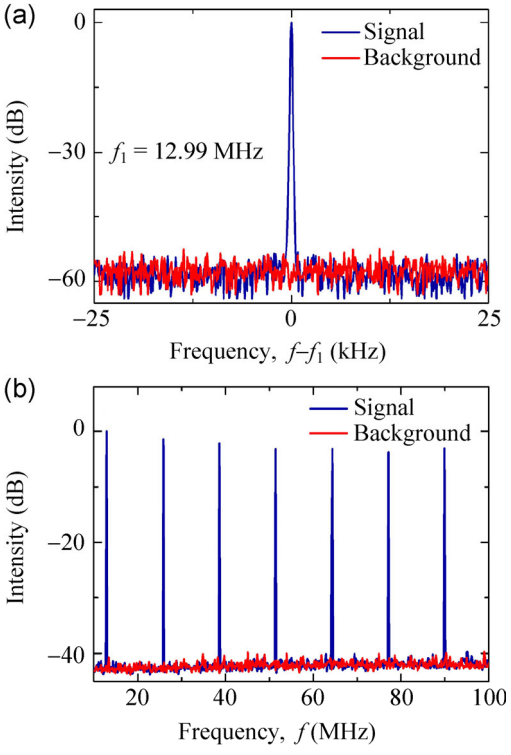

Figure 9 Radio-frequency (RF) spectra. (a) The fundamental frequency on a 50 kHz span and (b) the cavity harmonics on a 90 MHz span, with the red trace showing the noise floor of the RF analyzer.

4 Conclusion

We have fabricated a free-standing MoS_2–polymer composite by liquid phase exfoliation of chemically pristine MoS_2 and used this to mode-lock a fiber laser. Self-starting, stable picosecond pulses were generated, tunable in wavelength from 1,535 to 1,565 nm. Our results contribute to a growing body of work focused on studying the nonlinear optical properties of MoS_2, in particular at photon energies below the material bandgap, suggesting new opportunities in ultrafast photonics for this and other two-dimensional TMDs such as WS_2, $MoSe_2$, and $MoTe_2$.

Acknowledgements

MZ wishes to acknowledge funding from the EPSRC (EP/K03705), RCTH from the EPSRC (EP/G037221/1), GH from a CSC Cambridge International Scholarship, EJRK from the Royal Academy of Engineering (RAEng), through a RAEng Fellowship and TH from the RAEng (Graphlex).

References

[1] Liu, X.; Si, J.; Chang, B.; Xu, G.; Yang, Q.; Pan, Z.; Xie, S.; Ye, P.; Fan, J.; Wan, M. Third-order optical nonlinearity of the carbon nanotubes. *Appl. Phys. Lett.* **1999**, *74*, 164–166.

[2] Hendry, E.; Hale, P. J.; Moger, J.; Savchenko, A. K.; Mikhailov, S. A. Coherent nonlinear optical response of graphene. *Phys. Rev. Lett.* **2010**, *105*, 097401.

[3] Brida, D.; Tomadin, A.; Manzoni, C.; Kim, Y. J.; Lombardo, A.; Milana, S.; Nair, R. R.; Novoselov, K. S.; Ferrari, A. C.; Cerullo, G.; et al. Ultrafast collinear scattering and carrier multiplication in graphene. *Nat. Commun.* **2013**, *4*, 1987.

[4] Tomadin, A.; Brida, D.; Cerullo, G.; Ferrari, A. C.; Polini, M. Nonequilibrium dynamics of photoexcited electrons in graphene: collinear scattering, auger processes, and the impact of screening. *Phys. Rev. B* **2013**, *88*, 035430.

[5] Hasan, T.; Sun, Z.; Wang, F.; Bonaccorso, F.; Tan, P. H.; Rozhin, A. G.; Ferrari, A. C. Nanotube-polymer composites

for ultrafast photonics. *Adv. Mater.* **2009**, *21*, 3874–3899.

[6] Sun, Z.; Hasan, T.; Torrisi, F.; Popa, D.; Privitera, G.; Wang, F.; Bonaccorso, F.; Basko, D. M.; Ferrari, A. C. Graphene A. *ACS Nano* **2010**, *4*, 803–810.

[7] Set, S. Y.; Yaguchi, H.; Tanaka, Y.; Jablonski, M.; Sakakibara, Y.; Rozhin, A.; Tokumoto, M.; Kataura, H.; Achiba, Y.; Kikuchi, K. Mode-locked fiber lasers based on a saturable absorber incorporating carbon nanotubes. *In OSA Trends in Optics and Photonics (TOPS), Optical Fiber Communication Conference*; Washington, D.C., 2003; p. 44.

[8] Bao, Q.; Zhang, H.; Wang, Y.; Ni, Z.; Yan, Y.; Shen, Z. X.; Loh, K. P.; Tang, D. Y. Atomic-layer graphene as a saturable absorber for ultrafast pulsed lasers. *Adv. Funct. Mater.* **2009**, *19*, 3077–3083.

[9] Zhang, H.; Tang, D. Y.; Zhao, L. M.; Bao, Q. L.; Loh, K. P. Large energy mode locking of an erbium-doped fiber laser with atomic layer graphene. *Opt. Express* **2009**, *17*, 17630–17635.

[10] Dean, J. J.; van Driel, H. M. Second harmonic generation from graphene and graphitic films. *Appl. Phys. Lett.* **2009**, *95*, 261910.

[11] De Dominicis, L.; Botti, S.; Asilyan, L. S.; Ciardi, R.; Fantoni, R.; Terranova, M. L.; Fiori, A.; Orlanducci, S.; Appolloni, R. Second- and third-harmonic generation in single-walled carbon nanotubes at nanosecond time scale. *Appl. Phys. Lett.* **2004**, *85*, 1418–1420.

[12] Chow, K. K.; Yamashita, S. Four-wave mixing in a single-walled carbon-nanotube-deposited d-shaped fiber and its application in tunable wavelength conversion. *Opt. Express* **2009**, *17*, 15608–15613.

[13] Bonaccorso, F.; Sun, Z.; Hasan, T.; Ferrari, A. C. Graphene photonics and optoelectronics. *Nat. Photonics* **2010**, *4*, 611–622.

[14] Hasan, M. Z.; Kane, C. L. Colloquium: Topological insulators. *Rev. Mod. Phys.* **2010**, *82*, 3045–3067.

[15] He, K.; Zhang, Y.; Chang, C.-Z.; Song, C.-L.; Wang, L.-L.; Chen, X.; Jia, J.-F.; Fang, Z.; Dai, X.; Shan, W.-Y.; et al. Crossover of the three-dimensional topological insulator Bi_2Se_3 to the two-dimensional limit. *Nat. Phys.* **2010**, *6*, 584–588.

[16] Wang, Q. H.; Kalantar-Zadeh, K.; Kis, A.; Coleman, J. N.; Strano, M. S. Electronics and optoelectronics of two-dimensional transition metal dichalcogenides. *Nat. Nanotechnol.* **2012**, *7*, 699–712.

[17] Bonaccorso, F.; Sun, Z. Solution processing of graphene, topological insulators and other 2D crystals for ultrafast photonics. *Opt. Mater. Express* **2014**, *4*, 63–78.

[18] Bonaccorso, F.; Lombardo, A.; Hasan, T.; Sun, Z.; Colombo, L.; Ferrari, A. C. Production and processing of graphene and 2D crystals. *Mater. Today* **2012**, *15*, 564–589.

[19] Xu, M.; Liang, T.; Shi, M.; Chen, H. Graphene-like two-dimensional materials. *Chem. Rev.* **2013**, *113*, 3766–3798.

[20] Naguib, M.; Mochalin, V. N.; Barsoum, M. W.; Gogotsi, Y. MXenes: A new family of two-dimensional materials. *Adv. Mater.* **2014**, *26*, 992–1005.

[21] Mak, K. F.; Lee, C.; Hone, J.; Shan, J.; Heinz, T. F. Atomically Thin MoS_2: A new direct-gap semiconductor. *Phys. Rev. Lett.* **2010**, *105*, 136805.

[22] Wang, R.; Chien, H.-C.; Kumar, J.; Kumar, N.; Chiu, H.-Y.; Zhao, H. Third-harmonic generation in ultrathin films of MoS_2. *ACS Appl. Mater. Interfaces* **2014**, *6*, 314–318.

[23] Wang, K.; Wang, J.; Fan, J.; Lotya, M.; O'Neill, A.; Fox, D.; Feng, Y.; Zhang, X.; Jiang, B.; Zhao, Q.; et al. Ultrafast saturable absorption of two-dimensional MoS_2 nanosheets. *ACS Nano* **2013**, *7*, 9260–9267.

[24] Wang, K.; Feng, Y.; Chang, C.; Zhan, J.; Wang, C.; Zhao, Q.; Coleman, J. N.; Zhang, L.; Blau, W.; Wang, J. Broadband ultrafast nonlinear absorption and nonlinear refraction of layered molybdenum dichalcogenide semiconductors. *Nanoscale* **2014**, *6*, 10530–10535.

[25] Shi, H.; Yan, R.; Bertolazzi, S.; Brivio, J.; Gao, B.; Kis, A.; Jena, D.; Xing, H. G.; Huang, L. Exciton dynamics in suspended monolayer and few-layer MoS_2 2D crystals. *ACS Nano* **2013**, *7*, 1072–1080.

[26] Wang, R.; Ruzicka, B. A.; Kumar, N.; Bellus, M. Z.; Chiu, H.-Y.; Zhao, H. Ultrafast and spatially resolved studies of charge carriers in atomically thin molybdenum disulfide. *Phys. Rev. B* **2012**, *86*, 045406.

[27] Martinez, A.; Sun, Z. Nanotube and graphene saturable absorbers for fibre lasers. *Nat. Photonics* **2013**, *7*, 842–845.

[28] Wang, S.; Yu, H.; Zhang, H.; Wang, A.; Zhao, M.; Chen, Y.; Mei, L.; Wang, J. Broadband few-layer MoS_2 saturable absorbers. *Adv. Mater.* **2014**, *26*, 3538–3544.

[29] Torrisi, F.; Hasan, T.; Wu, W.; Sun, Z.; Lombardo, A.; Kulmala, T. S.; Hsieh, G.-W.; Jung, S.; Bonaccorso, F.; Paul, P. J.; et al. Inkjet-printed graphene electronics. *ACS Nano* **2012**, *6*, 2992–3006.

[30] Coleman, J. N.; Lotya, M.; O'Neill, A.; Bergin, S. D.; King, P. J.; Khan, U.; Young, K.; Gaucher, A.; De, S.; Smith, R. J.; et al. Two-dimensional nanosheets produced by liquid exfoliation of layered materials. *Science* **2011**, *331*, 568–571.

[31] Smith, R. J.; King, P. J.; Lotya, M.; Wirtz, C.; Khan, U.; De, S.; O'Neill, A.; Duesberg, G. S.; Grunlan, J. C.; Moriarty, G.; et al. Large-scale exfoliation of inorganic layered compounds in aqueous surfactant solutions. *Adv. Mater.* **2011**, *23*, 3944–3948.

[32] Joensen, P.; Frindt, R. F.; Morrison, S. R. Single-layer MoS_2. *Mater. Res. Bull.* **1986**, *21*, 457–461.

[33] Liu, K.-K.; Zhang, W.; Lee, Y.-H.; Lin, Y.-C.; Chang, M.-T.; Su, C.-Y.; Chang, C.-S.; Li, H.; Shi, Y.; Zhang, H.; et al.

Growth of large-area and highly crystalline MoS_2 thin layers on insulating substrates. *Nano Lett.* **2012**, *12*, 1538–1544.

[34] Lee, Y.-H.; Zhang, X.-Q.; Zhang, W.; Chang, M.-T.; Lin, C.-T.; Chang, K.-D.; Yu, Y.-C.; Wang, J. T.-W.; Chang, C.-S.; Li, L.-J.; et al. Synthesis of large-area MoS_2 atomic layers with chemical vapor deposition. *Adv. Mater.* **2012**, *24*, 2320–2325.

[35] Lee, Y.-H.; Yu, L.; Wang, H.; Fang, W.; Ling, X.; Shi, Y.; Lin, C.-T.; Huang, J.-K.; Chang, M.-T.; Chang, C.-S.; et al. Synthesis and transfer of single-layer transition metal disulfides on diverse surfaces. *Nano Lett.* **2013**, *13*, 1852–1857.

[36] Woodward, R. I.; Kelleher, E. J.; Runcorn, T. H.; Popov, S. V.; Torrisi, F.; Howe, R. T.; Hasan, T. Q-switched fiber laser with MoS_2 saturable absorber. In *CLEO*: *2014*; OSA: Washington, D.C., 2014; p. SM3H.6.

[37] Hasan, T.; Torrisi, F.; Sun, Z.; Popa, D.; Nicolosi, V.; Privitera, G.; Bonaccorso, F.; Ferrari, A. C. Solution-phase exfoliation of graphite for ultrafast photonics. *Phys. Status Solidi* **2010**, *247*, 2953–2957.

[38] Withers, F.; Yang, H.; Britnell, L.; Rooney, A.; Lewis, E.; Felten, A.; Woods, C.; Sanchez Romaguera, V.; Georgiou, T.; Eckmann, A.; et al. Heterostructures produced from nanosheet-based inks. *Nano Lett.* **2014**, *14*, 3987–3992.

[39] Secor, E. B.; Prabhumirashi, P. L.; Puntambekar, K.; Geier, M. L.; Hersam, M. C. Inkjet printing of high conductivity, flexible graphene patterns. *J. Phys. Chem. Lett.* **2013**, *4*, 1347–1351.

[40] Zhang, H.; Lu, S. B.; Zheng, J.; Du, J.; Wen, S. C.; Tang, D. Y.; Loh, K. P. Molybdenum disulfide (MoS_2) as a broadband saturable absorber for ultra-fast photonics. *Opt. Express* **2014**, *22*, 7249–7260.

[41] Sun, Z.; Hasan, T.; Ferrari, A. C. Ultrafast lasers mode-locked by nanotubes and graphene. *Phys. E Low-dimensional Syst. Nanostructures* **2012**, *44*, 1082–1091.

[42] Cunning, B. V.; Brown, C. L.; Kielpinski, D. Low-loss flake-graphene saturable absorber mirror for laser mode-locking at sub-200-fs pulse duration. *Appl. Phys. Lett.* **2011**, *99*, 261109.

[43] Sun, Z.; Popa, D.; Hasan, T.; Torrisi, F.; Wang, F.; Kelleher, E. J. R.; Travers, J. C.; Nicolosi, V.; Ferrari, A. C. A stable, wideband tunable, near transform-limited, graphene-mode-locked, Ultrafast Laser. *Nano Res.* **2010**, *3*, 653–660.

[44] Wang, F.; Rozhin, A. G.; Scardaci, V.; Sun, Z.; Hennrich, F.; White, I. H.; Milne, W. I.; Ferrari, A. C. Wideband-tuneable, nanotube mode-locked, fibre laser. *Nat. Nanotechnol.* **2008**, *3*, 738–742.

[45] Eda, G.; Yamaguchi, H.; Voiry, D.; Fujita, T.; Chen, M.; Chhowalla, M. Photoluminescence from chemically exfoliated MoS_2. *Nano Lett.* **2011**, *11*, 5111–5116.

[46] Gordon, R.; Yang, D.; Crozier, E.; Jiang, D.; Frindt, R. Structures of exfoliated single layers of WS_2, MoS_2, and $MoSe_2$ in aqueous suspension. *Phys. Rev. B* **2002**, *65*, 125407.

[47] Liu, H.; Luo, A.-P.; Wang, F.-Z.; Tang, R.; Liu, M.; Luo, Z.-C.; Xu, W.-C.; Zhao, C.-J.; Zhang, H. Femtosecond pulse erbium-doped fiber laser by a few-layer MoS_2 saturable absorber. *Opt. Lett.* **2014**, *39*, 4591–4594.

[48] Xia, H.; Li, H.; Lan, C.; Li, C.; Zhang, X.; Zhang, S.; Liu, Y. Ultrafast erbium-doped fiber laser mode-locked by a CVD-grown molybdenum disulfide (MoS_2) saturable absorber. *Opt. Express* **2014**, *22*, 17341–17348.

[49] Woodward, R. I.; Kelleher, E. J. R.; Howe, R. C. T.; Hu, G.; Torrisi, F.; Hasan, T.; Popov, S. V.; Taylor, J. R. Tunable Q-switched fiber laser based on saturable edge-state absorption in few-layer molybdenum disulfide (MoS_2). *Opt. Express* **2014**, In Press.

[50] Roxlo, C. B.; Chianelli, R. R.; Deckman, H. W.; Ruppert, A. F.; Wong, P. P. Bulk and surface optical absorption in molybdenum disulfide. *J. Vac. Sci. Technol. A Vacuum, Surfaces, Film.* **1987**, *5*, 555–557.

[51] Sun, Z.; Hasan, T.; Torrisi, F.; Popa, D.; Privitera, G.; Wang, F.; Bonaccorso, F.; Basko, D. M.; Ferrari, A. C. Graphene Mode-locked ultrafast laser. *ACS Nano* **2010**, *4*, 803–810.

[52] Hernandez, Y.; Lotya, M.; Rickard, D.; Bergin, S. D.; Coleman, J. N. Measurement of multicomponent solubility parameters for graphene facilitates solvent discovery. *Langmuir* **2010**, *26*, 3208–3213.

[53] Cunningham, G.; Lotya, M.; Cucinotta, C. S.; Sanvito, S.; Bergin, S. D.; Menzel, R.; Shaffer, M. S. P.; Coleman, J. N. Solvent exfoliation of transition metal dichalcogenides: Dispersibility of exfoliated nanosheets varies only weakly between Compounds. *ACS Nano* **2012**, *6*, 3468–3480.

[54] Hernandez, Y.; Nicolosi, V.; Lotya, M.; Blighe, F. M.; Sun, Z.; De, S.; McGovern, I. T.; Holland, B.; Byrne, M.; Gun'Ko, Y. K.; et al. High-yield production of graphene by liquid-phase exfoliation of graphite. *Nat. Nanotechnol.* **2008**, *3*, 563–568.

[55] Material safety data sheet for *N*-methyl-pyrrolidone. Sigma Aldrich.

[56] Israelachvili, J. N. *Intermolecular and Surface Forces*; 3rd ed.; Academic Press: Boston, 2011.

[57] Coleman, J. N. Liquid-phase exfoliation of nanotubes and graphene. *Adv. Funct. Mater.* **2009**, *19*, 3680–3695.

[58] Lotya, M.; Hernandez, Y.; King, P. J.; Smith, R. J.; Nicolosi, V.; Karlsson, L. S.; Blighe, F. M.; De, S.; Wang, Z.; McGovern, I. T.; et al. Liquid phase production of graphene by exfoliation of graphite in surfactant/water solutions. *J. Am. Chem. Soc.* **2009**, *131*, 3611–3620.

[59] Bonaccorso, F.; Zerbetto, M.; Ferrari, A. C.; Amendola, V. Sorting nanoparticles by centrifugal fields in clean media. *J. Phys. Chem. C* **2013**, *117*, 13217–13229.

[60] Beal, A.; Knights, J.; Liang, W. Transmission spectra of some transition metal dichalcogenides. II. Group VIA: Trigonal prismatic coordination. *J. Phys. C Solid State Phys.* **1972**, *5*, 3540.

[61] Bromley, R.; Murray, R.; Yoffe, A. The band structures of some transition metal dichalcogenides. III. Group VIA: Trigonal prism materials. *J. Phys. C Solid State Phys.* **1972**, *5*, 759.

[62] Wilson, J. A.; Yoffe, A. D. The transition metal dichalcogenides discussion and interpretation of the observed optical, electrical and structural properties. *Adv. Phys.* **1969**, *18*, 193–335.

[63] O'Neill, A.; Khan, U.; Coleman, J. Preparation of high concentration dispersions of exfoliated MoS_2 with increased flake size. *Chem. Mater.* **2012**, *24*, 2414–2421.

[64] Material safety data sheet for cyclohexanone. Sigma Aldrich.

[65] Lee, C.; Yan, H.; Brus, L. E.; Heinz, T. F.; Hone, J.; Ryu, S. Anomalous lattice vibrations of single- and few-layer MoS_2. *ACS Nano* **2010**, *4*, 2695–2700.

[66] Li, H.; Zhang, Q.; Yap, C. C. R.; Tay, B. K.; Edwin, T. H. T.; Olivier, A.; Baillargeat, D. From bulk to monolayer MoS_2: Evolution of Raman scattering. *Adv. Funct. Mater.* **2012**, *22*, 1385–1390.

[67] Zhang, X.; Han, W.; Wu, J.; Milana, S.; Lu, Y.; Li, Q.; Ferrari, A. C.; Tan, P. Raman spectroscopy of shear and layer breathing modes in multilayer MoS_2. *Phys. Rev. B* **2013**, *87*, 115413.

[68] Liang, L.; Meunier, V. First-principles Raman spectra of MoS_2, WS_2 and their heterostructures. *Nanoscale* **2014**, *6*, 5394–5401.

[69] Bohren, C. F.; Huffman, D. R. *Absorption and Scattering of Light by Small Particles*; Wiley: , 1998.

[70] Sheik-Bahae, M.; Said, A. A.; Wei, T.H.; Hagan, D. J.; Van Stryland, E. W. Sensitive measurement of optical nonlinearities using a single beam. *IEEE J. Quantum Electron.* **1990**, *26*, 760–769.

[71] Garmire, E. Resonant optical nonlinearities in semiconductors. *IEEE J. Sel. Top. Quantum Electron.* **2000**, *6*, 1094–1110.

[72] Boyd, R. W. *Nonlinear Optics*; Academic Press: , 2003.

[73] Mollenauer, L.; Gordon, J.; Islam, M. Soliton propagation in long fibers with periodically compensated loss. *IEEE J. Quantum Electron.* **1986**, *22*, 157–173.

[74] Hasegawa, A.; Tappert, F. Transmission of stationary nonlinear optical pulses in dispersive dielectric fibers. I. Anomalous dispersion. *Appl. Phys. Lett.* **1973**, *23*, 142–144.

[75] Von der Linde, D. Characterization of the noise in continuously operating mode-locked lasers. *Appl. Phys. B* **1986**, *39*, 201–217